



Fabrication of copper-cobalt heterostructures confined inside N-doped carbon nanocages for long-lasting Zn-air batteries

Yanrong Ren^{a,1}, Pengcheng Ye^{a,1}, Jiadong Chen^{b,1}, Haiyan Wang^{a,**}, Jiqiang Ning^c, Junling Shen^a, Yijun Zhong^a, Yong Hu^{a,d,*}

^a Key Laboratory of the Ministry of Education for Advanced Catalysis Materials, Department of Chemistry, Zhejiang Normal University, Jinhua, 321004, China

^b Institute of Catalysis, Department of Chemistry, Zhejiang University, Hangzhou, 310028, China

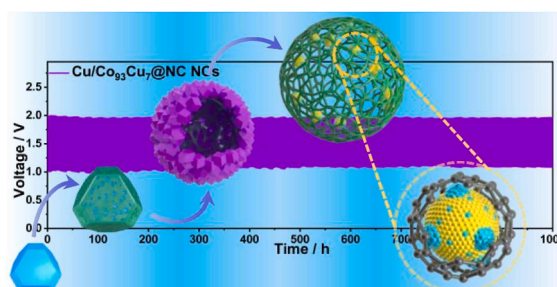
^c Department of Optical Science and Engineering, Fudan University, Shanghai, 200438, China

^d Hangzhou Institute of Advanced Studies, Zhejiang Normal University, Hangzhou, Zhejiang, 311231, China

HIGHLIGHTS

- An efficient Cu/Co₉₃Cu₇@NC NCs catalyst is designed for ORR and OER.
- The hollow architecture enhances the electrocatalytic kinetics.
- DFT verifies that N-C, Cu and Co cooperatively improve the intrinsic activity.
- The as-assembled Zn-air batteries exhibit excellent activity and durability.

GRAPHICAL ABSTRACT



ARTICLE INFO

Keywords:

Cu
Co₉₃Cu₇
Nanoparticles
N-doped carbon nanocage
Zn-air batteries

ABSTRACT

Delicate construction of sophisticated bimetallic nanostructures provides a favorable way to boost the efficiency of bifunctional electrocatalysts for oxygen reduction reaction (ORR) and oxygen evolution reaction (OER), which is critical to the fabrication of rechargeable Zn-air batteries. Herein, hetero-structured Cu/Co₉₃Cu₇ nanoparticles confined inside N-doped carbon nanocages (denoted as Cu/Co₉₃Cu₇@NC NCs) are fabricated through a facile “MOF-in situ-reduction and in situ-growth-MOF” strategy. Benefiting from the unique hollow architecture and superior intrinsic activity of the optimized interfaces, the as-prepared catalyst displays an appealing electrocatalytic performance including a positive half-wave potential ($E_{1/2}$) of 0.88 V for ORR and a low OER overpotential of 262 mV at 10 mA cm⁻². Theoretical calculations further disclose the key role of the rationally designed Co/Cu/N-doped carbon heterostructures, which significantly reduces the energy barrier for *OOH formation and eventually promotes the ORR. Rechargeable Zn-air batteries assembled with the Cu/Co₉₃Cu₇@NC NCs exhibit a large specific capacity of 884.9 mAh g_{Zn}⁻¹ and a maximum power density of 225.9 mW cm⁻². Moreover, the assembled batteries are stable for 1000 h during the long-term charge and discharge cycling, demonstrating the great promise for practical applications.

* Corresponding author. Key Laboratory of the Ministry of Education for Advanced Catalysis Materials, Department of Chemistry, Zhejiang Normal University, Jinhua, 321004, China.,

** Corresponding author.

E-mail addresses: chemwhy@zjnu.edu.cn (H. Wang), yonghu@zjnu.edu.cn, yonghuzjnu@163.com (Y. Hu).

¹ These authors contributed equally to this work.

<https://doi.org/10.1016/j.jpowsour.2022.231908>

Received 17 May 2022; Received in revised form 16 July 2022; Accepted 29 July 2022

Available online 11 August 2022

0378-7753/© 2022 Elsevier B.V. All rights reserved.

1. Introduction

The rising epidemic of energy shortage and environmental crisis has stimulated enormous research on sustainable and efficient energy storage and conversion technologies [1–3]. Rechargeable Zn-air batteries are considered as one of the promising candidates due to its high energy density, low cost, environmental friendliness, and high safety [4,5]. The bottleneck still is the slow reaction kinetics of the multi-electron and proton coupled oxygen reduction/evolution process at the air cathode, leading to insufficient power and short lifespan [6,7]. At present, precious metals remain the most active catalysts toward oxygen reduction reaction (ORR) and oxygen evolution reaction (OER), but the scarcity, poor bifunctionality, and inferior durability terribly restrict their practical applications in rechargeable Zn-air batteries [8–10].

In this context, efforts have been devoted to developing novel and durable transition metal-based electrocatalysts for ORR and OER, attributing to their low cost and natural abundance [11–17]. Among them, Cu-based materials have received considerable attention, in view of the harmonious biomimetic chemistry with oxygen [18–20]. “Volcano plot” reveals that among all the non-noble metals, Cu shows the closest position to the top Pt, indicating its superb activity towards ORR [21]. Previous studies have also demonstrated Cu-based materials are excellent ORR catalysts, but the inferior intrinsic activity for OER is the major obstacle to their applications in Zn-air batteries [22–26]. Usually, incorporation of a foreign metal to fabricate bimetallic catalysts has been demonstrated efficacious to fulfill a bifunctionality [27–31]. Such a bimetallic system can preserve the inherent properties of the separate metals, and offer more opportunities to change the electronic structure and reduce the kinetic energy barriers through the cooperative interaction, thus accelerating the ORR and OER processes [27,30].

The design of efficient bimetallic nanomaterials requires the rational comprehending of the compositional and microstructural design principles, as well as the sophisticated manipulation of the geometric architecture of bimetallic nanostructures [32–36]. Recent studies have highlighted the outstanding potential of hetero-nanostructured bimetal catalysts for oxygen electrocatalysis owing to their superior intrinsic activity [20,37–39]. Nevertheless, due to the distinct diffusion properties of the various metal cations, it is immensely difficult to precisely control the nanoscale arrangement of CuM (M represents a foreign transition metal) dual metals, and these nanoparticles tend to aggregation and surface oxidation during the high-temperature pyrolysis. Thus, there are yet few works on the rational design of advanced CuM (M represents a foreign transition metal) nanostructures for ORR and OER, and their bifunctional activity is still far from satisfactory. Furthermore, it is challengeable to probe the intrinsic bimetallic synergetic effect, as well as identify the real active structure and elucidate the underlying synergetic catalytic mechanism of Cu-based dual-metal catalysts on account of the complexity of the bimetallic structures.

In addition to the nanoscale arrangement of bimetal, catalyst morphology has shown important consequences for the electrocatalytic properties. Hollow nanostructures featuring with large specific surface area, high permeability, open diffusion channels and reduced ionic diffusion paths, are pivotal to expose more active sites to electrolytes and oxygen gas, which are highly desirable for ORR and OER [40–43]. Moreover, the inner hollow cavity can provide the local microenvironment to alter the coordination or adsorption of reactants/intermediates. In recent years, metal-organic frameworks (MOFs) represent appealing precursors for the synthesis of hollow nanoarchitectures [44,45]. The wise selection of organic ligands and metal ions/clusters bestows unique topological structures and special physicochemical properties over MOFs, which offers great flexibility for constructing advanced bimetallic catalysts with sophisticated hollow structure, complex compositions, and favorable electrochemical performances, but presents a major challenge.

Considering the above, we propose a facile “MOF-in situ-reduction and in situ-growth-MOF” strategy to fabricate hetero-structured Cu/

Co₉₃Cu₇ nanoparticles confined inside N-doped carbon nanocages (denoted as Cu/Co₉₃Cu₇@NC NCs). Starting from truncated Cu-BTC polyhedra (BTC stands for benzene-1,3,5-tricarboxylic acid), the intermediate of Cu/polydopamine (PDA)@CoCu-ZIF is prepared through consecutive PDA coating, etching, and coprecipitation processes, and finally converted into Cu/Co₉₃Cu₇@NC NCs after a pyrolysis procedure. Interestingly, in this synthesis, PDA not only avails the reduction of Cu²⁺ to Cu clusters during the PDA coating, but also acts as the protector to control the hollow structure, as well as provides the nitrogen sources to increase the number of active sites, ultimately contributing to the formation of bimetal-embedded N-doped carbon nanocages. The advantages of the exceptional carbon chain-woven nanocage-like superstructure are further highlighted by the comprehensive improvements in the bifunctional electrocatalytic performance. As evidenced, a positive half-wave potential (E_{1/2}) of 0.88 V towards ORR and a low OER overpotential of 262 mV to reach 10 mA cm⁻² are achieved with the as-obtained catalyst. Theoretical calculations further unravel the key role of the N-doped carbon, Cu and Co heterostructures in lowering the formation energy barrier for *OOH intermediates, thus improving the intrinsic activity. When assembling for a liquid Zn-air battery, the device acquires a large specific capacity of 884.9 mAh g_{Zn}⁻¹ and a high power density of 225.9 mW cm⁻², along with long-lasting life-time over 1000 h, holding great promise for practical applications in energy storage and conversion systems.

2. Experimental

2.1. Synthesis of Cu-BTC

0.9 g of Cu(NO₃)₂·3H₂O and 0.4 g of polyvinylpyrrolidone (PVP) were dissolved in 50 mL of methanol and sonicated for 5 min to obtain a blue solution. Then 50 mL of methanol solution containing 0.43 g of BTC was added into the above solution and stirred for 10 min. The mixed solution was further aged at room temperature for 24 h. The resulting blue precipitate was collected by centrifugation and further washed several times with methanol and ethanol in turn.

2.2. Synthesis of Cu/Cu-BTC@PDA

0.06 g of Cu-BTC was dispersed into 75 mL of methanol via sonication. Then 15 mL of methanol solution containing dopamine hydrochloride (20 mM) was added into the above solution, followed by stirring at 60 °C for 7 h. Finally, the product was obtained by centrifuging and washing with methanol and ethanol in turn, which was denoted as Cu/Cu-BTC@PDA.

2.3. Synthesis of Cu/PDA@CoCu-ZIF

75 mg of Cu/Cu-BTC@PDA was dispersed in 25 mL of 2-methylimidazole (2-MIM, 0.4 M) methanol solution to form Solution A. And 0.3639 g of Co(NO₃)₂·6H₂O (0.05 M) was dispersed in 25 mL of methanol solution to obtain Solution B. Then solution B was added into Solution A and further aged at room temperature for 1 h. After centrifugation, the purple precipitate, denoted as Cu/PDA@CoCu-ZIF, was collected.

2.4. Synthesis of Cu/Co₉₃Cu₇@NC NCs

The Cu/PDA@CoCu-ZIF was annealed in N₂ atmosphere at 800 °C for 2 h to prepare the black product, which was labeled as Cu/Co₉₃Cu₇@NC NCs.

2.5. Synthesis of Cu@NC NSs and Co@NC NPHs

For comparison, Cu/Cu-BTC@PDA was directly annealed in N₂ atmosphere at 800 °C for 2 h. The as-obtained product was labeled as

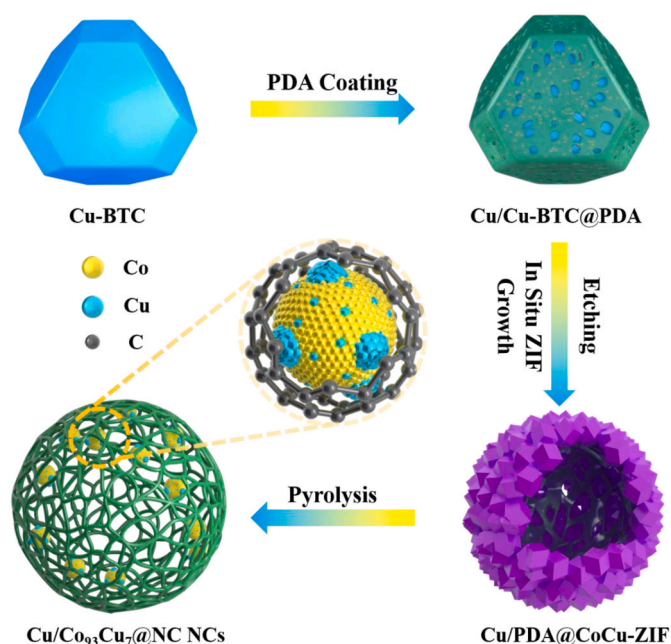


Fig. 1. Schematic illustration of the fabrication of the Cu/Co₉₃Cu₇@NC NCs through a "MOF-in situ-reduction and in situ-growth-MOF" strategy.

Cu@NC NPs. 25 mL of Co(NO₃)₂·6H₂O methanol solution (0.05 M) was added into 25 mL of 2-MIM (0.4 M) methanol solution and then aged at room temperature for 1 h. The purple precipitate of ZIF-67 was collected after centrifugation and washing with methanol and ethanol in turn. Co@NC NPs were then prepared by annealing ZIF-67 in N₂ atmosphere with the same pyrolysis process of Cu/Co₉₃Cu₇@NC NCs.

2.6. Characterizations

The compositions of the as-prepared samples were characterized by the powder X-ray diffraction (XRD) using a Bruker D8 Advance diffractometer equipped with Cu-Kα radiation source. Field emission scanning electron microscopy (FESEM) and energy dispersive X-ray (EDX) spectroscopy were measured on a Hitachi S-4800 scanning electron microanalyzer with an accelerating voltage of 15 kV. Transmission electron microscopy (TEM) and high-resolution TEM (HRTEM) images were obtained with a JEM-2100F microscope operated at 200 kV. The structural disorder of the products was evaluated using Raman tests, which were conducted on a Renishaw in Via-Reflex with a laser excitation at 532 nm. The N₂ adsorption-desorption experiments were carried out on an autosorb iQ automated gas sorption analyzer. X-ray photoelectron spectroscopy (XPS) was conducted on an ESCALab MKII X-ray photoelectron spectrometer using Mg Kα X-ray as the excitation source.

The electrochemical measurements, the assembly of Zn-air batteries, and computation details can be seen in the supporting information.

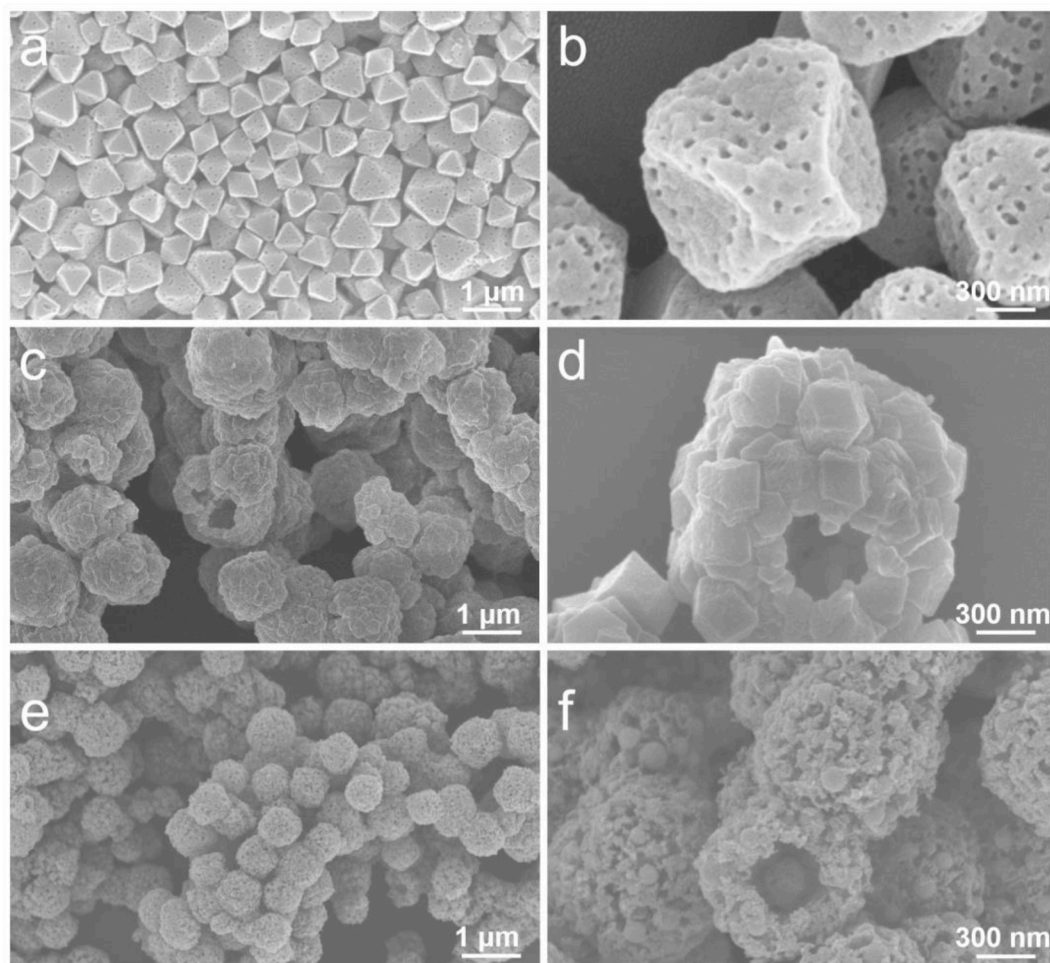


Fig. 2. FESEM images of the (a, b) Cu/Cu-BTC@PDA; (c, d) Cu/PDA@CoCu-ZIF and (e, f) Cu/Co₉₃Cu₇@NC NCs.

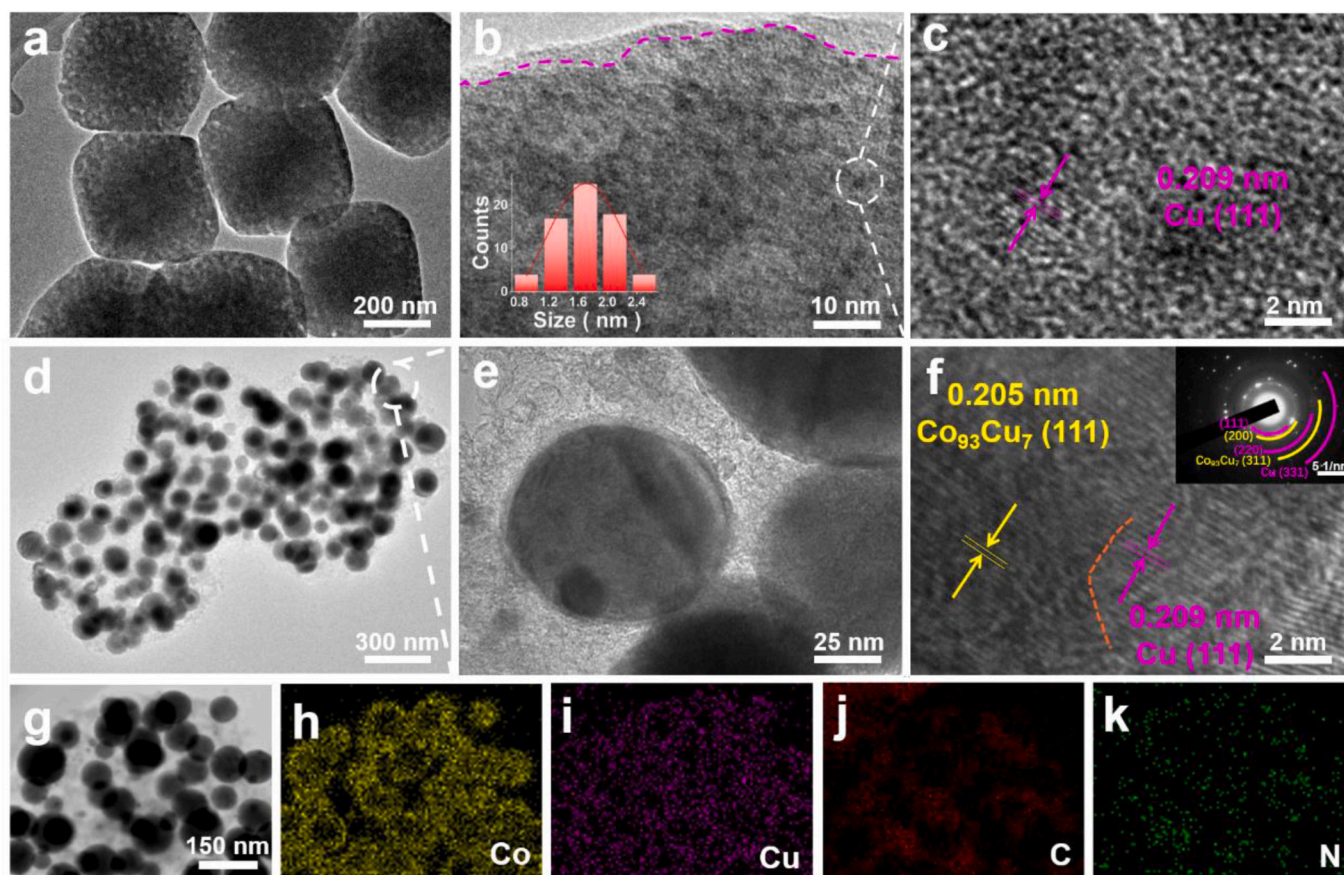


Fig. 3. (a, b) TEM images and (c) HRTEM image of the Cu/Cu-BTC@PDA. (d, e) TEM images and (f) HRTEM image with an inset of the SAED pattern, (g–k) STEM image and corresponding elemental mapping images for Co, Cu, C, and N of the Cu/Co₉₃Cu₇@NC NCs.

3. Results and discussion

3.1. Synthesis and characteristics of the Cu/Co₉₃Cu₇@NC NCs

The synthetic process for the fabrication of Cu/Co₉₃Cu₇@NC NCs through a “MOF-in situ-reduction and in situ-growth-MOF” strategy is illustrated in Fig. 1. Uniform Cu-BTC nanocrystals are first synthesized as the sacrificial templates, which further convert into the dusty blue precipitates of the Cu/Cu-BTC encapsulated with PDA after the polymerization reaction of dopamine (Fig. S1). Afterwards, the Cu/Cu-BTC@PDA is successfully transformed to the intermediate of purple Cu/PDA@CoCu-ZIF through partial etching and coprecipitation. The formed Cu clusters could serve as the seeds to induce the formation of the intermediate Cu–H species with a strong reducing ability [46–48]. During the following pyrolysis procedure, the 2-MIM is converted to N-doped carbon shell, and the cobalt and copper ions can be reduced by carbon or reduced gas released by MOF decomposition under pyrolysis in N₂, resulting in the formation of Cu/Co₉₃Cu₇@NC NCs.

The morphological and structural evolution of Cu/Co₉₃Cu₇@NC NCs is monitored by different methods. FESEM image shows that the as-prepared Cu-BTC nanocrystals exhibit the uniform truncated octahedral morphologies with an average size of about 500 nm (Fig. S2). After polymerization reactions, the Cu/Cu-BTC@PDA well inherits the truncated octahedral shape of the Cu-BTC, but reveal a porous surface (Fig. 2a, b and 3a). XRD pattern of Cu/Cu-BTC@PDA shows the same diffraction peaks of Cu-BTC but a lower peak intensity, indicating the successful growth of PDA on the Cu-BTC nanocrystals (Fig. S3). TEM images also manifest the PDA films coating uniformly on the octahedral Cu-BTC surfaces. And simultaneously, due to the relative positive reduction potentials of $\phi^0\text{Cu}^{2+}/\text{Cu}$ (+0.34 eV vs. SHE), ultrasmall Cu

clusters with the size of 1–2 nm are easily reduced by dopamine, which exhibit a homogenous distribution on the matrix (Fig. 3b and c) [49]. Further reacting Cu/Cu-BTC@PDA with Co(NO₃)₂ and 2-methylimidazole (2-MIM) leads to the hollow interior and the coprecipitation of CoCu-ZIF on the surface of PDA simultaneously (Fig. 2c and d). As shown in the XRD pattern of Cu/PDA@CoCu-ZIF, only the characteristic peaks of CoCu-ZIF can be observed, indicating the full consumption of Cu-BTC during the process (Fig. S4) [50]. To investigate the formation mechanism of hollow cavities, Cu/Cu-BTC@PDA is treated with Co(NO₃)₂ and 2-MIM in methanol solutions, respectively. As shown in the FESEM images, the solid octahedral morphology of Cu/Cu-BTC@PDA was intactly maintained after immersion into Co(NO₃)₂ solution, whereas these octahedra are partially etched by 2-MIM, leaving the octahedral cage-like architecture (Fig. S5). These phenomena clearly demonstrate that the hollow interior of Cu/PDA@CoCu-ZIF is fabricated under the etching action of 2-MIM, on account of the stronger coordination ability of 2-MIM in comparison with BTC. Additionally, PDA coating is crucial to the hollow structure, as no hollow spheres can be found when using pure Cu-BTC as the precursor (Fig. S6). Thus, it can be concluded that during the subsequent reaction of Cu/Cu-BTC@PDA with Co(NO₃)₂ and 2-MIM, the BTC ligand is in situ exchanged with the 2-MIM gradually, and the Cu²⁺ and Co²⁺ ions can be coordinated with the 2-MIM ligands, eventually forming Cu/PDA@CoCu-ZIF. After the thermal annealing, Cu/PDA@CoCu-ZIF is converted to the Cu/Co₉₃Cu₇@NC NC composite, which exhibits a unique nanocage-like morphology with an average diameter of about 750 nm (Fig. 2e and f). A megascopic FESEM image further reveals that these nanocages are woven of carbon chains with plenty of nanoparticles embedded (Fig. 2f). EDX spectra for Co, Cu, N, C and O also verifies the successful fabrication of the composite of Cu/Co₉₃Cu₇@NC NCs (Fig. S7).

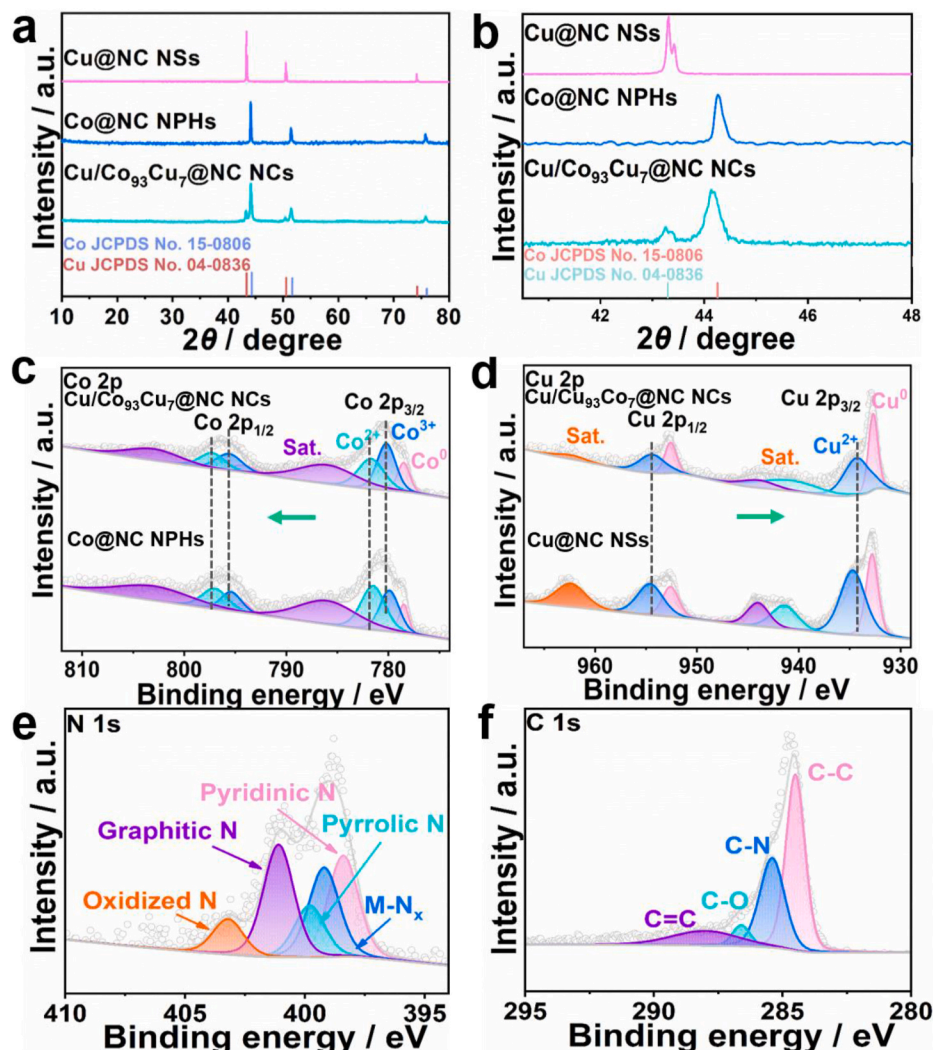


Fig. 4. (a) XRD patterns of the Cu/Co₉₃Cu₇@NC NCs, Cu@NC NSs and Co@NC NPHs. High-resolution XPS spectra for (c) Co 2p of the Cu/Co₉₃Cu₇@NC NCs and Co@NC NPHs, (d) Cu 2p of the Cu/Co₉₃Cu₇@NC NCs and Cu@NC NSs, (e) N 1s and (f) C 1s for the Cu/Co₉₃Cu₇@NC NCs.

The porous nanocage-like architecture of Cu/Co₉₃Cu₇@NC NCs is further confirmed by TEM (Fig. 3d). As shown in Fig. 3e, a large amount of metal nanoparticles is confined inside the carbon nanocages. HRTEM image of these highly faceted nanoparticles displays two plane spacings, in which the lattice fringe of 0.209 nm is assigned to the (111) crystal plane of Cu, while the plane spacing of 0.205 nm is located between the Co (111) and Cu (111) planes, indicating an alloy structure. These clearly demonstrate the heterostructure of Cu/Co₉₃Cu₇ (Fig. 3f). The selected area electron diffraction (SAED) image also certifies the coexistence of metallic Cu and Co₉₃Cu₇ in the particles (Inset of Fig. 3f). Moreover, the differentiated distributions of Cu, Co, C and N elements throughout the nanocage distinctly confirm the precise construction of Cu/Co₉₃Cu₇@NC NCs (Fig. 3g–k). The uniform distribution of the metal particles can be ascribed to the strong interactions between 2-MIM ligands and metal ions, as well as the strong force between reduced Cu with PDA, can help avoid the aggregation of metal nanoparticles into large chunks and expose abundant active sites.

To reveal the superiority of the Cu/Co₉₃Cu₇@NC NCs, the contrast samples of Cu embedded in nitrogen-doped nanospheres (denoted as Cu@NC NSs) and Co embedded in nitrogen-doped nano-polyhedrons (denoted as Co@NC NPHs) are fabricated by pyrolyzing Cu/Cu-BTC@PDA and ZIF-67 in inert nitrogen atmosphere at 800 °C for 2 h, respectively (Fig. S8). Fig. S9 shows the FESEM images of the two samples, in which the Cu@NC NSs exhibit the nanosphere-like structure,

while the Co@NC NPHs intactly inherit the polyhedral morphology of ZIF-67.

The phase structures of the various samples were then analyzed by XRD measurements. As shown in Fig. 4a, the distinguishable diffraction peaks of the Cu/Co₉₃Cu₇@NC NCs at 43.3°, 50.4°, and 74.1° correspond well to metallic Cu (JCPDS No. 04-0836). Besides, the other peaks are consistently located near the positions of the (111), (200), and (220) planes of metallic Co (JCPDS No. 15-0806). Nevertheless, the peak of Co (111) plane shifts towards a lower diffraction angle that is 44.1°, indicating an alloy structure (Fig. 4b). According to Vegard's Law, the atomic content of Cu in the alloy is roughly estimated to be 7%. Raman spectra of the Cu/Co₉₃Cu₇@NC NCs, Cu@NC NSs and Co@NC NPHs samples all display the D and G bands centered at around 1350 and 1580 cm⁻¹, which reflect the structural defects and graphitization degree in the materials, respectively (Fig. S10). Compared to Cu@NC NSs and Co@NC NPHs, Cu/Co₉₃Cu₇@NC NCs possess a higher intensity ratio between D band and G band (I_D/I_G), suggesting more structural defects existing in the carbon skeleton.

To further get into the interaction between Cu and Co₉₃Cu₇, XPS was conducted. The survey spectrum evidences the coexistence of Co, Cu, C, N, and O elements in Cu/Co₉₃Cu₇@NC NCs (Fig. S11). The high-resolution Co 2p XPS spectrum exhibits the main peaks of metallic Co (778.5 eV and 794 eV), Co³⁺ (780.2 eV and 795.6 eV), and Co²⁺ (781.5 eV and 797.25 eV) with two satellite peaks at 786.0 eV and 803.0 eV

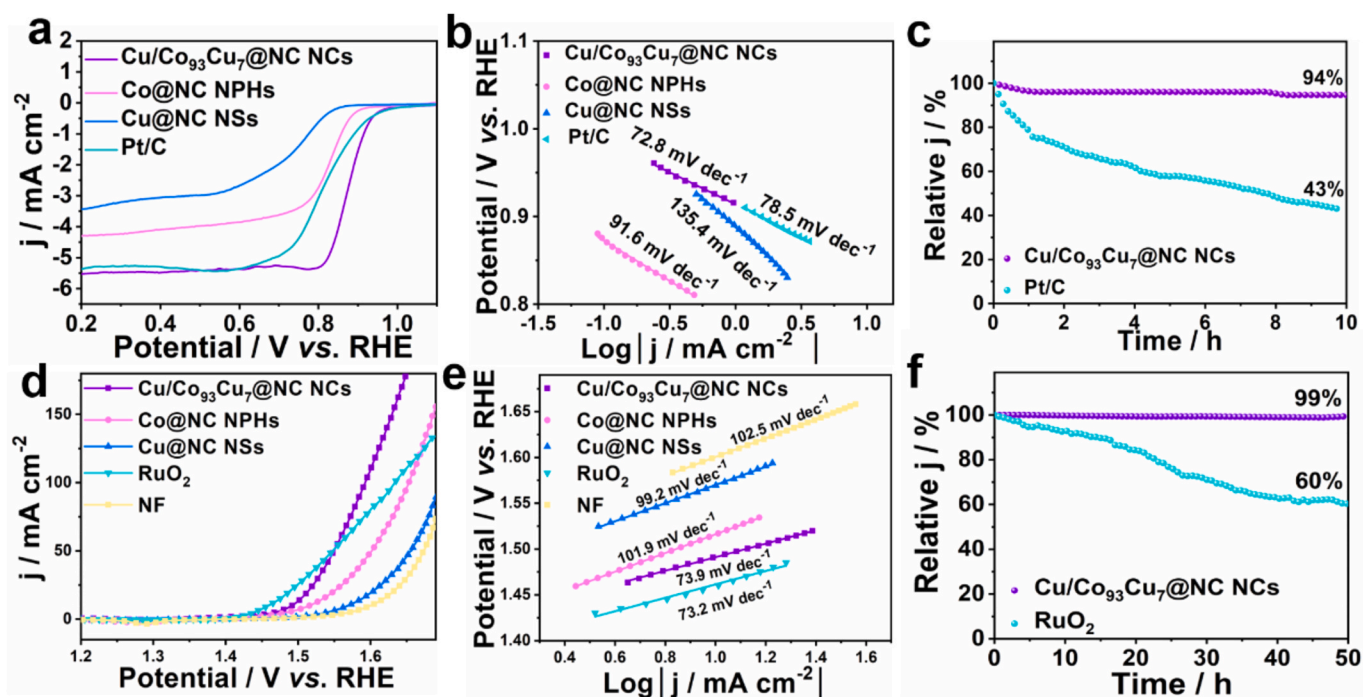


Fig. 5. Evaluation of the ORR and OER performances of the Cu/Co₉₃Cu₇@NC NCs, Co@NC NPHs, Cu@NC NSs and commercial Pt/C or RuO₂ as well as NF catalysts. (a) ORR polarization curves. (b) Tafel plots for ORR. (c) ORR chronoamperometric response of the Cu/Co₉₃Cu₇@NC NCs and Pt/C. (d) Polarization curves and (e) Tafel plots for OER. (f) OER chronopotentiometric response of the Cu/Co₉₃Cu₇@NC NCs and RuO₂ at a current density of 10 mA cm⁻².

(Fig. 4c) [35,51]. Compared to that of Co@NC NPHs, the Co 2p XPS spectrum of Cu/Co₉₃Cu₇@NC NCs up-shifts to a higher binding energy, indicating the electron-deficient property. In the Cu 2p XPS spectrum, the peaks at 932.8 eV and 952.6 eV correspond to the metallic Cu, while the peaks appear at 934.3 eV and 954.2 eV are assigned to Cu 2p_{3/2} and Cu 2p_{1/2} of Cu²⁺ (Fig. 4d) [52,53]. Furthermore, the peaks of Cu²⁺ in Cu/Co₉₃Cu₇@NC NCs negatively shift to a lower binding energy concerning those of Cu@NC NSs, suggesting the electron-rich state. These results combined further confirm a strong electron transfer from Co to Cu at the Cu/Co₉₃Cu₇ interface. The electron-deficient Co can activate the surrounding carbon, enhance the electron transfer around the Co–N–C sites, and modulate the adsorption and deprotonation of oxygen intermediates, thus accelerating electron transfer kinetics [54]. The N 1s XPS spectrum is deconvoluted to five peaks, which are assigned to pyridinic N (398.4 eV), Metal-N_x (M-N_x, 399.2 eV), pyrrolic N (399.8 eV), graphitic N (401.1 eV), and oxidized N (403.2 eV, Fig. 4e) [55]. Evidently, the contents of pyridinic-N and M-N_x in Cu/Co₉₃Cu₇@NC NCs are higher than those in Co@NC NPHs (Fig. S12 and Table S1), and therefore Cu/Co₉₃Cu₇@NC NCs can provide more active sites for ORR and OER. In the C 1s spectra, the peak at 285.4 eV is attributed to C–N bond, verifying the successful doping of N in the carbon matrix (Fig. 4f and Fig. S13) [7].

N₂ adsorption-desorption isotherms of the Cu/Co₉₃Cu₇@NC NCs show the type-IV curves with an evident hysteresis loop, indicating the presence of abundant mesopores in the carbon shells (Fig. S14). The pore size distribution indicates the mesopores centered at a diameter of 3.4 nm. The sharp increase of the adsorption capacity in the high-pressure regions (0.8 < P/P₀ < 1.0) also validates the existence of rich macropores in Cu/Co₉₃Cu₇@NC NCs due to the porous nanocage-like architecture. Notably, the coexistence of mesopores and macropores with the large specific surface area of 93.4 m² g⁻¹ are favorable for mass transport at the triple interface, thus boosting their electrocatalytic efficiency [56].

3.2. Electrocatalytic performance towards ORR and OER

The electrocatalytic ORR performances of the Cu/Co₉₃Cu₇@NC NCs, Co@NC NPHs and Cu@NC NSs were initially evaluated with a three-electrode configuration. As shown in Fig. S15, the cyclic voltammetry (CV) curve of Cu/Co₉₃Cu₇@NC NCs exhibits a characteristic oxygen reduction peak in the O₂-saturated 0.1 M KOH solution rather than N₂-saturated electrolyte, indicating its outstanding activity towards ORR. Polarization curves reveal that the ORR activity of the Cu/Co₉₃Cu₇@NC NCs surpasses the others with the relatively positive onset (E₀) and half-wave potentials (E_{1/2}) of 0.94 V and 0.88 V, respectively (Fig. 5a and Fig. S16). The values are comparable or superior to those of the previously reported bifunctional electrocatalysts (Table S2). The fast ORR kinetics of the Cu/Co₉₃Cu₇@NC NCs is further confirmed by the smaller Tafel slope (72.8 mV dec⁻¹) compared to Co@NC NPHs (91.6 mV dec⁻¹), Cu@NC NSs (135.4 mV dec⁻¹) and Pt/C catalysts (78.5 mV dec⁻¹) (Fig. 5b). Moreover, the reaction mechanism of the Cu/Co₉₃Cu₇@NC NCs for ORR is analyzed by Koutecky-Levich (K-L) equation, which shows an apparent four-electron transfer process from 0.3 to 0.7 V (Fig. S17). In addition, rotating ring-disk electrode (RRDE) measurement validates the number of electrons transferred (n) is about 3.95, and the H₂O₂ yield is less than 10% (Fig. S18). As shown in Fig. 5c, the Cu/Co₉₃Cu₇@NC NCs exhibit 6% of current loss after 10 h of continuous operation, while only 43% of the initial current is maintained for Pt/C catalyst. The excellent durability of Cu/Co₉₃Cu₇@NC NCs towards ORR is also elucidated by the linear sweep voltammetry (LSV) curves with a negligible attenuation of E_{1/2} after stability tests (Fig. S19).

As shown in Fig. 5d, the Cu/Co₉₃Cu₇@NC NCs can deliver a current density of 10 mA cm⁻² at the overpotential of 262 mV, which is slightly higher than that of RuO₂ catalyst (230 mV), and significantly lower than those of Co@NC NPHs (286 mV), Cu@NC NSs (339 mV) and Ni foam (NF) (370 mV). The value is also comparable to the most of the state-of-the-art OER catalysts (Table S3). Additionally, the Cu/Co₉₃Cu₇@NC NCs exhibit the lowest Tafel slope of 73.9 mV dec⁻¹ among the catalysts, which is comparable to that of RuO₂ (73.2 mV dec⁻¹). This further demonstrates the expedited OER kinetics in the Cu/Co₉₃Cu₇@NC NCs

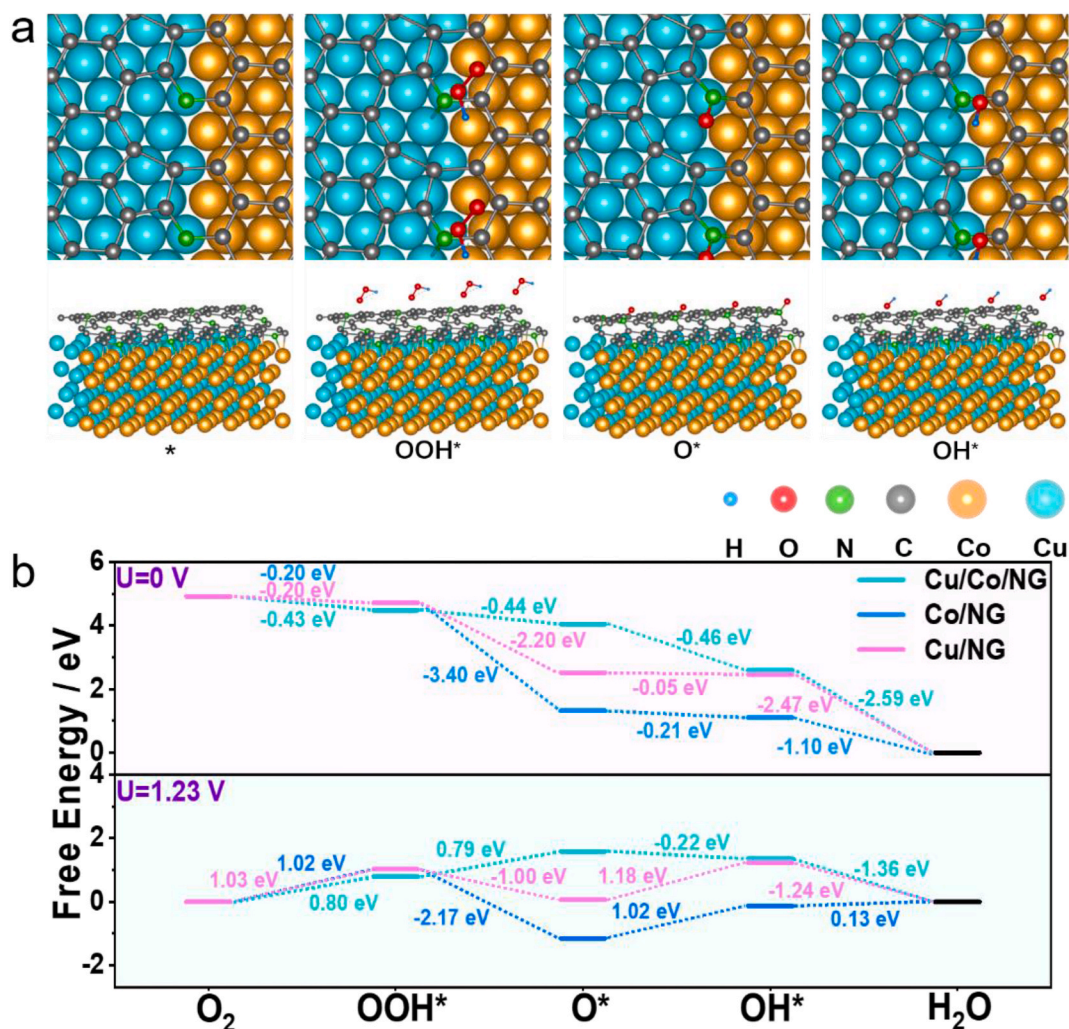


Fig. 6. (a) Optimized atomic structures of *O , *OOH , *O , and *OH on Cu/Co/NG. (b) Gibbs free energy diagram for ORR processes on the Cu/Co/NG, Co/NG and Cu/NG at $U = 0$ V and $U = 1.23$ V.

(Fig. 5e). This aligns well with the electrochemical impedance spectroscopy (EIS) with the smallest charge transfer resistance for Cu/Co₉₃Cu₇@NC NCs (Fig. S20 and Table S4). The superior activity and reaction kinetics of the Cu/Co₉₃Cu₇@NC NCs arise from the larger electrochemical active surface area (ECSA), as proven by the higher double-layer capacitance (C_{dl}) of 47.2 mF cm⁻². It adequately attests that Cu/Co₉₃Cu₇@NC NCs with the hollow nanostructure can expose more available active sites to electrolytes to boost the reactions (Fig. S21). To further identify the intrinsic activity from the compositions, the polarization curves were normalized by the ECSA. As displayed in Fig. S22, the Cu/Co₉₃Cu₇@NC NCs display a larger normalized current density compared to the other samples, indicating that the synergistic effect of Cu, Co₉₃Cu₇ and N-doped carbon dominate their superb intrinsic activity towards OER. Remarkably, the current of the Cu/Co₉₃Cu₇@NC NCs can maintain 50 h with negligible decrease, while only 60% of the current is maintained for the RuO₂ catalyst, further confirming their outstanding durability (Fig. 5f and Fig. S23). Such excellent stability can be ascribed to the robust structural and chemical stability with Cu/Co₉₃Cu₇ nanoparticles encapsulated by N-doped carbon cages, which drastically inhibit metals from the aggregation and loss during the long-term test.

3.3. DFT calculations

To obtain an insight into the catalytic mechanism of the Cu/

Co₉₃Cu₇@NC NCs, DFT calculations were performed on the Co/NG, Cu/NG, Cu/Co/NG models. We calculated the free energy of the oxygen intermediates (*OOH , *O , and *OH) on the above models to infer the surface reaction process, and the optimized adsorption sites for the intermediates are the graphite surface (Fig. 6a, Fig. S24 and Fig. S25). The Gibbs free energy diagrams for ORR processes on the Co/NG, Cu/NG, Cu/Co/NG are depicted in Fig. 6b. When U is set to 0 V, the free energy of each ORR reaction step for the Co/NG, Cu/NG, Cu/Co/NG is downhill, indicating a spontaneous reaction. With regard to $U = 1.23$ V, the first reduction step in which *OOH is formed from O_2 displays a distinct upward trend, causing it to be the rate-determining step. The energy barrier of *OOH formation for Cu/Co/NG is calculated to be 0.80 eV, which is lower than those of Co/NG (1.02 eV) and Cu/NG (1.03 eV). This clearly demonstrates that the synergistic effect of Co, Cu and N-doped carbon significantly accelerates the *OOH formation process, thus endowing the Cu/Co₉₃Cu₇@NC NCs with remarkable activity towards ORR.

3.4. Electrochemical performances of liquid and solid-state Zn-air batteries

The potential difference between half-wave potential of ORR and OER potential at 10 mA cm⁻² (ΔE) was used to evaluate the bifunctionality of the as-prepared catalysts. The Cu/Co₉₃Cu₇@NC NCs obtain a ΔE value of 0.612 V, which is considerably lower than the comparative

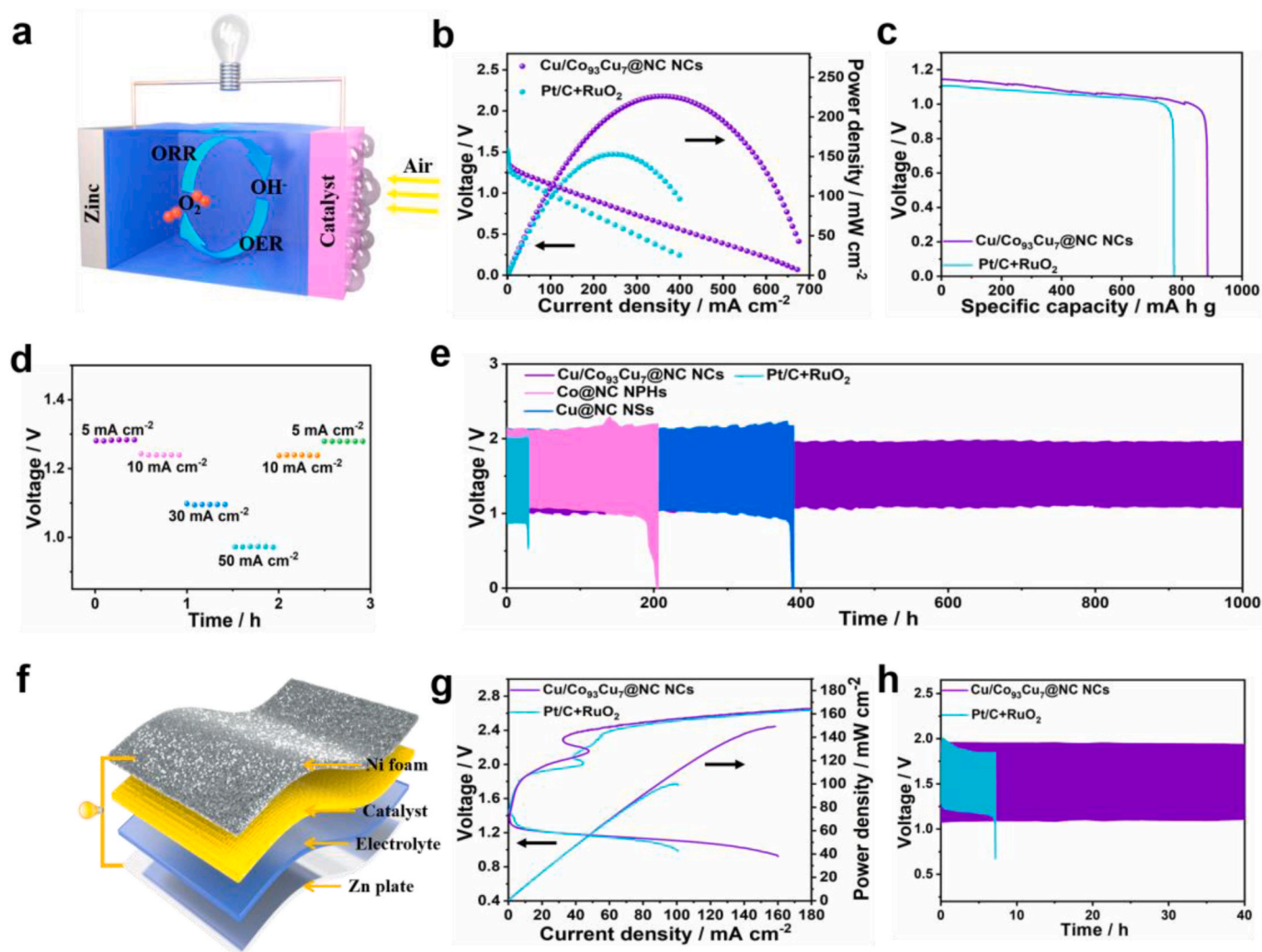


Fig. 7. (a) Schematic configuration of the liquid rechargeable Zn-air battery. (b) Discharge polarization curves and power density curves of liquid Zn-air batteries based on the Cu/Co₉₃Cu₇@NC NCs and Pt/C + RuO₂ catalysts. (c) Specific capacities of liquid Zn-air batteries based on the Cu/Co₉₃Cu₇@NC NCs and Pt/C + RuO₂ catalysts. (d) Discharge voltage plateaus of the Cu/Co₉₃Cu₇@NC NCs-based liquid Zn-air battery at various current densities. (e) Cycling performances of liquid Zn-air batteries based on the Cu/Co₉₃Cu₇@NC NCs, Co@NC NPHs, Cu@NC NSs and Pt/C + RuO₂ catalysts. (f) Schematic configuration of the solid-state rechargeable Zn-air battery. (g) Charge and discharge polarization curves, and power density of the solid-state Zn-air batteries based on Cu/Co₉₃Cu₇@NC NCs and Pt/RuO₂ catalysts. (h) Cycling performance of the solid-state Zn-air batteries based on Cu/Co₉₃Cu₇@NC NCs and Pt/RuO₂ catalysts.

materials and those of the previously reported catalysts (Fig. S26 and Table S5). Furthermore, a liquid rechargeable Zn-air battery was assembled using Zn foil as the anode, the catalyst as air cathode, and 6 M KOH containing 0.2 M Zn (AC)₂ as the electrolyte (Fig. 7a). As shown in Fig. S27, the liquid Zn-air battery delivers a steady open-circuit voltage of 1.52 V. Fig. 7b compares the discharge curves of the Cu/Co₉₃Cu₇@NC NCs and Pt/C + RuO₂ catalysts, and a maximum power density of 225.9 mW cm⁻² is achieved for the Cu/Co₉₃Cu₇@NC NCs, being 1.5 times as high as Pt/C + RuO₂ catalysts (152.9 mW cm⁻²). This result also outperforms most of the recently reported bifunctional catalysts (Table S6). The battery can also reach a high specific capacity of 884.9 mAh g_{Zn}⁻¹ at the current density of 20 mA cm⁻², corresponding to an energy density of 989.2 Wh kg_{Zn}⁻¹, which are superior to Pt/C + RuO₂-based device (733.2 mAh g_{Zn}⁻¹ and 848.9 Wh kg_{Zn}⁻¹, Fig. 7c and Fig. S28). Moreover, Cu/Co₉₃Cu₇@NC NCs exhibits stable discharge voltage plateaus at different current densities from 5 to 50 mA cm⁻², indicating a good rate performance and excellent reversibility (Fig. 7d). Notably, the battery with Cu/Co₉₃Cu₇@NC NCs demonstrates a long-lasting cycle life of 1000 h with negligible voltage fading, while the Pt/C + RuO₂ cathode shows fast decay for less than 50 h (Fig. 7e). This value also outperforms Co@NC NPHs (200 h) and Cu@NC NSs-based devices (380 h) as well as

most reported Zn-air batteries, further evidencing the robust stability of the Cu/Co₉₃Cu₇@NC NCs (Table S6). Fig. 7f depicts the schematic configuration of solid-state rechargeable Zn-air batteries, in which the Cu/Co₉₃Cu₇@NC NCs is served as the cathode, Zn foil as the anode, and an alkaline gel polymer as the electrolyte. The solid-state battery driven by Cu/Co₉₃Cu₇@NC NCs delivers a stable open-circuit voltage of 1.39 V, and a higher peak power density of 149.0 mW cm⁻² than that of Pt/C + RuO₂ catalysts (Fig. S29 and Fig. 7g). Besides, the galvanostatic discharge-charge profiles exhibits no obvious drop after continuous operation for 40 h, suggesting its robust electrochemical stability (Fig. 7h). In contrast, the solid-state Zn-air battery assembled with Pt/C + RuO₂ catalysts can only maintain 7 h. Two solid-state Zn-air batteries connected in series can power a LED light, manifesting its great potential in actual applications (Fig. S30).

4. Conclusion

In summary, we have demonstrated the purposely construction of Cu/Co₉₃Cu₇@NC NCs for rechargeable Zn-air batteries through a “MOF-in situ-reduction and in situ-growth-MOF” strategy. The as-obtained catalyst manifests excellent bifunctional performance towards both

ORR and OER, and thus achieve a maximum power density of 225.9 mW cm⁻² and robust cycle life over 1000 h when assembled for a rechargeable Zn-air battery. The distinguished performance can be accredited to the unique nanocage-like architecture with fast mass transportation, the robust structural and chemical stability using carbon encapsulation, as well as the lowered formation energy of *OOH stemming from the synergistic effect of Cu, Co₉₃Cu₇ and N-doped carbon, as evidenced by the experimental and DFT results. This strategy can provide a path for design and fabrication of effective and long-lasting bimetal-based electrocatalysts with complex components and ingenious structures for highly efficient rechargeable Zn-air batteries.

CRedit authorship contribution statement

Yanrong Ren: Formal analysis, Conceptualization, Investigation, Methodology. **Pengcheng Ye:** Formal analysis, Conceptualization, Investigation, Methodology, Software. **Jiadong Chen:** DFT calculation. **Haiyan Wang:** Conceptualization, Writing – review & editing, Data curation, Methodology, Investigation, Validation. **Jiqiang Ning:** Formal analysis. **Junling Shen:** Writing – review & editing. **Yijun Zhong:** Formal analysis. **Yong Hu:** Conceptualization, Supervision, Funding acquisition, Writing – review & editing.

Declaration of competing interest

The authors declare that they have no known competing financial interests or personal relationships that could have appeared to influence the work reported in this paper.

Data availability

The authors do not have permission to share data.

Acknowledgements

This work is financially supported by the Major Program of Zhejiang Provincial Natural Science Foundation of China (LD22B030002), Zhejiang Provincial Ten Thousand Talent Program (2021R51009) and the Independent Designing Scientific Research Project of Zhejiang Normal University (2020ZS03). H. Wang acknowledges the Self Designed Scientific Research of Zhejiang Normal University (2021ZS0604).

Appendix A. Supplementary data

Supplementary data to this article can be found online at <https://doi.org/10.1016/j.jpowsour.2022.231908>.

References

- N.T. Suen, S.F. Hung, Q. Quan, N. Zhang, Y.J. Xu, H.M. Chen, Electrocatalysis for the oxygen evolution reaction: recent development and future perspectives, *Chem. Soc. Rev.* 46 (2017) 337–365, <https://doi.org/10.1039/c6cs00328a>.
- X. Xu, S. W. S. Guo, K.S. Hui, J. Ma, D.A. Dinh, K.N. Hui, H. Wang, L. Zhang, G. Zhou, Cobalt phosphosulfide nanoparticles encapsulated into heteroatom-doped carbon as bifunctional electrocatalyst for Zn-air battery, *Adv. Powder Mater.* 1 (2022), 100027, <https://doi.org/10.1016/j.apmater.2021.12.003>.
- H. Wang, W. Ye, Y. Yang, Y. Zhong, Y. Hu, Zn-ion hybrid supercapacitors: achievements, challenges and future perspectives, *Nano Energy* 85 (2021), 105942, <https://doi.org/10.1016/j.nanoen.2021.105942>.
- J. Fu, Z.P. Cano, M.G. Park, A. Yu, M. Fowler, Z. Chen, Electrically rechargeable zinc-air batteries: progress, challenges, and perspectives, *Adv. Mater.* 29 (2017), 1604685, <https://doi.org/10.1002/adma.201604685>.
- Z. Xu, L. Yan, H. Wang, J. S. X. Yang, J. Ning, Y. Zhong, Y. Hu, Hierarchical mesoporous S, N-codoped carbon nanostructures composed of Co/Co-CuS/carbon nanoplate arrays on carbon nanofibers as a self-supported air cathode for long-lasting rechargeable Zn-air batteries, *Sci. China Technol. Sci.* 65 (2022) 693–703, <https://doi.org/10.1007/s11431-021-1942-6>.
- Z. Liang, N. Kong, C. Yang, W. Zhang, H. Zheng, H. Lin, R. Cao, Highly curved nanostructure-coated Co, N-doped carbon materials for oxygen electrocatalysis, *Angew. Chem. Int. Ed.* 60 (2021) 12759–12764, <https://doi.org/10.1002/anie.202101562>.
- L. Yan, Z. Xu, W. Hu, J. Ning, Y. Zhong, Y. Hu, Formation of sandwiched leaf-like CNTs-Co/ZnCo₂O₄@NC-CNTs nanohybrids for high-power-density rechargeable Zn-air batteries, *Nano Energy* 82 (2021), 105710, <https://doi.org/10.1016/j.nanoen.2020.105710>.
- Y.J. Wang, W. Long, L. Wang, R. Yuan, A. Ignaszak, B. Fang, D.P. Wilkinson, Unlocking the door to highly active ORR catalysts for PEMFC applications: polyhedron-engineered Pt-based nanocrystals, *Energy Environ. Sci.* 11 (2018) 258–275, <https://doi.org/10.1039/c7ee02444d>.
- L. Zhang, H. Jang, H. Liu, M.G. Kim, D. Yang, S. Liu, X. Liu, J. Cho, Sodium-decorated amorphous/crystalline RuO₂ with rich oxygen vacancies: a robust pH-universal oxygen evolution electrocatalyst, *Angew. Chem. Int. Ed.* 60 (2021) 18821–18829, <https://doi.org/10.1002/anie.202106631>.
- Y. Jiao, C. Yang, H. Wang, Y. Zhong, Y. Hu, Optimization strategies on the advanced engineering of Co-based nanomaterials for electrochemical oxygen evolution, *J. Alloys Compd.* 890 (2022), 161929, <https://doi.org/10.1016/j.jallcom.2021.161929>.
- C.C. Hou, L. Zou, Y. Wang, Q. Xu, MOF-mediated fabrication of a porous 3D superstructure of carbon nanosheets decorated with ultrafine cobalt phosphide nanoparticles for efficient electrocatalysis and zinc-air batteries, *Angew. Chem. Int. Ed.* 59 (2020) 21360–21366, <https://doi.org/10.1002/anie.202011347>.
- L. Yan, H. Wang, J. Shen, J. Ning, Y. Zhong, Y. Hu, Formation of mesoporous Co/CoS/Metal-N-C@S, N-codoped hairy carbon polyhedrons as an efficient trifunctional electrocatalyst for Zn-air batteries and water splitting, *Chem. Eng. J.* 403 (2021), 126385, <https://doi.org/10.1016/j.cej.2020.126385>.
- H. Hu, L. Han, M. Yu, Z. Wang, X.W. Lou, Metal-organic-framework-engaged formation of Co nanoparticle-embedded carbon@Co₉S₈ double-shelled nanocages for efficient oxygen reduction, *Energy Environ. Sci.* 9 (2016) 107–111, <https://doi.org/10.1039/c5ee02903a>.
- F. Lu, M. Zhou, Y. Zhou, X. Zeng, First-row transition metal based catalysts for the oxygen evolution reaction under alkaline conditions: basic principles and recent advances, *Small* 13 (2017), 1701931, <https://doi.org/10.1002/smll.201701931>.
- H. Wang, Y. Jiao, S. Wang, P. Ye, J. Ning, Y. Zhong, Y. Hu, Accelerating triple transport in zinc-air batteries and water electrolysis by spatially confining Co nanoparticles in breathable honeycomb-like macroporous N-doped carbon, *Small* 17 (2021), 2103517, <https://doi.org/10.1002/smll.202103517>.
- H. Yang, S. Gao, D. Rao, X. Yan, Designing superior bifunctional electrocatalyst with high-purity pyrrole-type Co_N and adjacent metallic cobalt sites for rechargeable Zn-air batteries, *Energy Storage Mater.* 46 (2022) 553–562, <https://doi.org/10.1016/j.ensm.2022.01.040>.
- S. Gao, H. Yang, D. Rao, N. Wang, Y. Li, J. Li, S. Rao, C. Maouche, Z. Wu, B. Li, Y. Zhou, J. Yang, Supercritical CO₂ assisted synthesis of highly accessible iron single atoms and clusters on nitrogen-doped carbon as efficient oxygen reduction electrocatalysts, *Chem. Eng. J.* 433 (2022), 134460, <https://doi.org/10.1016/j.cej.2021.134460>.
- M. Jahan, Z. Liu, K.P. Loh, A graphene oxide and copper-centered metal organic framework composite as a tri-functional catalyst for HER, OER, and ORR, *Adv. Funct. Mater.* 23 (2013) 5363–5372, <https://doi.org/10.1002/adfm.201300510>.
- W. Cheng, Z.P. Wu, D. Luan, S.Q. Zang, X.W. Lou, Synergistic cobalt-copper-based bimetal-organic framework nanoboxes toward efficient electrochemical oxygen evolution, *Angew. Chem. Int. Ed.* 60 (2021) 26397–26402, <https://doi.org/10.1002/anie.202112775>.
- Q. Zhang, P. Kumar, X. Zhu, R. Daiyan, N.M. Bedford, K.H. Wu, Z. Han, T. Zhang, R. Amal, X. Lu, Electronically modified atomic sites within a multicomponent Co/Cu composite for efficient oxygen electroreduction, *Adv. Energy Mater.* 11 (2021), 100303, <https://doi.org/10.1002/aenm.202100303>.
- J.K. Nørskov, J. Rossmeisl, A. Logadottir, L. Lindqvist, J.R. Kitchin, T. Bligaard, H. Jónsson, Origin of the overpotential for oxygen reduction at a fuel-cell cathode, *J. Phys. Chem. B* 108 (2004) 17886–17892, <https://doi.org/10.1021/jp047349j>.
- L. Yang, H. Xu, H. Liu, X. Zeng, D. Cheng, Y. Huang, L. Zheng, R. Cao, D. Cao, Oxygen-reconstituted active species of single-atom Cu catalysts for oxygen reduction reaction, *Research* (2020), 7593023, <https://doi.org/10.34133/2020/7593023>, 2020.
- K. Iwase, T. Yoshioka, S. Nakanishi, K. Hashimoto, K. Kamiya, Copper-modified covalent triazine frameworks as non-noble-metal electrocatalysts for oxygen reduction, *Angew. Chem. Int. Ed.* 54 (2015) 11068–11072, <https://doi.org/10.1002/anie.201503637>.
- H. Wu, H. Li, X. Zhao, Q. Liu, J. Wang, J. Xiao, S. Xie, R. Si, F. Yang, S. Miao, X. Guo, G. Wang, X. Bao, Highly doped and exposed Cu(1)-N active sites within graphene towards efficient oxygen reduction for zinc-air batteries, *Energy Environ. Sci.* 9 (2016) 3736–3745, <https://doi.org/10.1039/c6ee01867j>.
- W. Li, C. Min, F. Tan, Z. Li, B. Zhang, R. Si, M. Xu, W. Liu, L. Zhou, Q. Wei, Y. Zhang, X. Yang, Bottom-up construction of active sites in a Cu-N₄-C catalyst for highly efficient oxygen reduction reaction, *ACS Nano* 13 (2019) 3177–3187, <https://doi.org/10.1021/acsnano.8b08692>.
- Q. Shi, C. Zhu, H. Zhong, D. Su, N. Li, M.H. Engelhard, H. Xia, Q. Zhang, S. Peng, S. P. Beckman, D. Du, Y. Lin, Nanovoid incorporated Ir_xCu metallic aerogels for oxygen evolution reaction catalysis, *ACS Energy Lett.* 3 (2018) 2038–2044, <https://doi.org/10.1021/acsenenergyltt.8b01338>.
- S. Wang, H. Wang, C. Huang, P. Ye, X. Luo, J. Ning, Y. Zhong, Y. Hu, Trifunctional electrocatalyst of N-doped graphitic carbon nanosheets encapsulated with CoFe alloy nanocrystals: the key roles of bimetal components and high-content graphitic-N, *Appl. Catal. B: Environ.* 298 (2021), 120512, <https://doi.org/10.1016/j.apcatb.2021.120512>.
- C. Liu, P. Zuo, Y. Jin, X. Zong, D. Li, Y. Xiong, Defect-enriched carbon nanofibers encapsulating NiCo oxide for efficient oxygen electrocatalysis and rechargeable Zn-

- air batteries, *J. Power Sources* 473 (2020), 228604, <https://doi.org/10.1016/j.jpowsour.2020.228604>.
- [29] Z. Li, H. Li, M. Li, J. Hu, Y. Liu, D. Sun, G. Fu, Y. Tang, Iminodiacetonitrile induce-synthesis of two-dimensional PdNi/Ni@carbon nanosheets with uniform dispersion and strong interface bonding as an effective bifunctional electrocatalyst in air-cathode, *Energy Storage Mater.* 42 (2021) 118–128, <https://doi.org/10.1016/j.ensm.2021.07.027>.
- [30] C. Li, M. Wu, R. Liu, High-performance bifunctional oxygen electrocatalysts for zinc-air batteries over mesoporous Fe/Co-N-C nanofibers with embedding FeCo alloy nanoparticles, *Appl. Catal. B: Environ.* 244 (2019) 150–158, <https://doi.org/10.1016/j.apcatb.2018.11.039>.
- [31] P. Liu, Y. Hu, X. Liu, T. Wang, P. Xi, S. Xi, D. Gao, J. Wang, Cu and Co nanoparticle-Co-decorated N-doped graphene nanosheets: a high efficiency bifunctional electrocatalyst for rechargeable Zn-air batteries, *J. Mater. Chem.* 7 (2019) 12851–12858, <https://doi.org/10.1039/c9ta02894c>.
- [32] S.Y. Lin, L.X. Xia, Y. Cao, H.L. Meng, L. Zhang, J.J. Feng, Y. Zhao, A.J. Wang, Electronic regulation of ZnCo dual-atomic active sites entrapped in 1D@2D hierarchical N-doped carbon for efficient synergistic catalysis of oxygen reduction in Zn-air battery, *Small* 28 (2022), 2107141, <https://doi.org/10.1002/sml.202107141>.
- [33] T. Chen, F. Tong, J. Enderlein, Z. Zheng, Plasmon-driven modulation of reaction pathways of individual Pt-modified Au nanorods, *Nano Lett.* 20 (2020) 3326–3330, <https://doi.org/10.1021/acs.nanolett.0c00206>.
- [34] Z. Zheng, T. Tachikawa, T. Majima, Plasmon-enhanced formic acid dehydrogenation using anisotropic Pd-Au nanorods studied at the single-particle level, *J. Am. Chem. Soc.* 137 (2015) 948–957, <https://doi.org/10.1021/ja511719g>.
- [35] C. Guan, A. Sumboja, W. Zang, Y. Qian, H. Zhang, X. Liu, Z. Liu, D. Zhao, S. J. Pennycook, J. Wang, Decorating Co/CoN_x nanoparticles in nitrogen-doped carbon nanoarrays for flexible and rechargeable zinc-air batteries, *Energy Storage Mater.* 16 (2019) 243–250, <https://doi.org/10.1016/j.ensm.2018.06.001>.
- [36] L. Bu, N. Zhang, S. Guo, X. Zhang, J. Li, J. Yao, T. Wu, G. Lu, J.Y. Ma, D. Su, X. Huang, Biaxially strained PtPb/Pt core/shell nanoplate boosts oxygen reduction catalysis, *Science* 354 (2016) 1410–1414, <https://doi.org/10.1126/science.aah6133>.
- [37] X. Wang, S.I. Choi, L.T. Ruling, M. Luo, C. Ma, L. Zhang, M. Chi, J. Liu, Z. Xie, J. A. Herron, M. Mavrikakis, Y. Xia, Palladium-platinum core-shell icosahedra with substantially enhanced activity and durability towards oxygen reduction, *Nat. Commun.* 6 (2015) 7594, <https://doi.org/10.1038/ncomms8594>.
- [38] H. Yin, D. Li, Z. Chi, Q. Zhang, X. Liu, L. Ding, S. Li, J. Liu, Z. Guo, L. Wang, Iridium coated Co nanoparticles embedded into highly porous N-doped carbon nanocubes grafted with carbon nanotubes as a catalytic cathode for high-performance Li-O₂ batteries, *J. Mater. Chem.* 9 (2021) 17865–17875, <https://doi.org/10.1039/d1ta04830a>.
- [39] S. Lin, Y. Chen, Y. Cao, L. Zhang, J.J. Feng, A.J. Wang, Aminouracil-assisted synthesis of CoFe decorated bougainvillea-like N-doped carbon nanoflowers for boosting Zn-air battery and water electrolysis, *J. Power Sources* 521 (2022), 230926, <https://doi.org/10.1016/j.jpowsour.2021.230926>.
- [40] Z. Wang, H. Jin, T. Meng, K. Liao, W. Meng, J. Yang, D. He, Y. Xiong, S. Mu, Fe, Cu-coordinated ZIF-derived carbon framework for efficient oxygen reduction reaction and zinc-air batteries, *Adv. Funct. Mater.* 28 (2018), <https://doi.org/10.1002/adfm.201802596>.
- [41] Y.P. Deng, Y. Jiang, D. Luo, R. Liang, S. Cheng, Z. Bai, Y. Liu, W. Lei, L. Yang, J. Zhu, Z. Chen, Hierarchical porous double-shelled electrocatalyst with tailored lattice alkalinity toward bifunctional oxygen reactions for metal-air batteries, *ACS Energy Lett.* 2 (2017) 2706–2712, <https://doi.org/10.1021/acsenerylett.7b00989>.
- [42] J. Zhang, L. Yu, Y. Chen, X.F. Lu, S. Gao, X.W. Lou, Designed formation of double-shelled Ni-Fe layered-double-hydroxide nanocages for efficient oxygen evolution reaction, *Adv. Mater.* 32 (2020), 1906432, <https://doi.org/10.1002/adma.201906432>.
- [43] L. Han, X.Y. Yu, X.W. Lou, Formation of prussian-blue-analog nanocages via a direct etching method and their conversion into Ni-Co-mixed oxide for enhanced oxygen evolution, *Adv. Mater.* 28 (2016) 4601–4605, <https://doi.org/10.1002/adma.201506315>.
- [44] T. Kwon, H. Hwang, Y.J. Sa, J. Park, H. Baik, S.H. Joo, K. Lee, Cobalt assisted synthesis of IrCu hollow octahedral nanocages as highly active electrocatalysts toward oxygen evolution reaction, *Adv. Funct. Mater.* 27 (2017), 1604688, <https://doi.org/10.1002/adfm.201604688>.
- [45] S. Liu, Z. Wang, S. Zhou, F. Yu, M. Yu, C.Y. Chiang, W. Zhou, J. Zhao, J. Qiu, Metal-organic-framework-derived hybrid carbon nanocages as a bifunctional electrocatalyst for oxygen reduction and evolution, *Adv. Mater.* 29 (2017), 1700874, <https://doi.org/10.1002/adma.201700874>.
- [46] B.Y. Guan, X.Y. Yu, H.B. Wu, X.W. Lou, Complex nanostructures from materials based on metal-organic frameworks for electrochemical energy storage and conversion, *Adv. Mater.* 29 (2017), 1703614, <https://doi.org/10.1002/adma.201703614>.
- [47] J.L. Sun, Y.Z. Chen, B.D. Ge, J.H. Li, G.M. Wang, Three-shell Cu@Co@Ni nanoparticles stabilized with a metal-organic framework for enhanced tandem catalysis, *ACS Appl. Mater. Interfaces* 11 (2019) 940–947, <https://doi.org/10.1021/acsami.8b18584>.
- [48] J.M. Yan, Z.L. Wang, H.L. Wang, Q. Jiang, Rapid and energy-efficient synthesis of a graphene-CuCo hybrid as a high performance catalyst, *J. Mater. Chem.* 22 (2012) 10990–10993, <https://doi.org/10.1039/c2jm31042b>.
- [49] Y. Xie, B. Yan, H. Xu, J. Chen, Q. Liu, Y. Deng, H. Zeng, Highly regenerable mussel-inspired Fe₃O₄@polydopamine-Ag core-shell microspheres as catalyst and adsorbent for methylene blue removal, *ACS Appl. Mater. Interfaces* 6 (2014) 8845–8852, <https://doi.org/10.1021/am501632f>.
- [50] H. Yang, X.W. He, F. Wang, Y. Kang, J. Zhang, Doping copper into ZIF-67 for enhancing gas uptake capacity and visible-light-driven photocatalytic degradation of organic dye, *J. Mater. Chem.* 22 (2012) 21849–21851, <https://doi.org/10.1039/c2jm35602c>.
- [51] F. Li, T. Qin, Y. Sun, R. Jiang, J. Yuan, X. Liu, A.P. O'Mullane, Preparation of a one-dimensional hierarchical MnO@CNT@Co-N/C ternary nanostructure as a high-performance bifunctional electrocatalyst for rechargeable Zn-air batteries, *J. Mater. Chem.* 9 (2021) 22533–22543, <https://doi.org/10.1039/d1ta07259e>.
- [52] J. Tian, D. Liu, J. Li, D. Sun, H. Liu, H. Wang, Y. Tang, Cu/Cu₂O nanoparticles core-regulated carbon catalyst for alkaline Al-air batteries, *Chin. Chem. Lett.* 32 (2021) 2427–2432, <https://doi.org/10.1016/j.ccl.2021.01.022>.
- [53] W. Lu, J. Shen, P. Zhang, Y. Zhong, Y. Hu, X.W. Lou, Construction of CoO/Co-Cu-S hierarchical tubular heterostructures for hybrid supercapacitors, *Angew. Chem. Int. Ed.* 58 (2019) 15441–15447, <https://doi.org/10.1002/anie.201907516>.
- [54] Y. Guo, P. Yuan, J. Zhang, Y. Hu, I.S. Amiin, X. Wang, J. Zhou, H. Xia, Z. Song, Q. Xu, S. Mu, Carbon nanosheets containing discrete Co-N_x-B_y-C active sites for efficient oxygen electrocatalysis and rechargeable Zn-air batteries, *ACS Nano* 12 (2018) 1894–1901, <https://doi.org/10.1021/acsnano.7b08721>.
- [55] S. Yuan, J. Zhang, L. Hu, J. Li, S. Li, Y. Gao, Q. Zhang, L. Gu, W. Yang, X. Feng, B. Wang, Decarboxylation-induced defects in MOF-derived single cobalt atom@ carbon electrocatalysts for efficient oxygen reduction, *Angew. Chem. Int. Ed.* 60 (2021) 21685–21690, <https://doi.org/10.1002/anie.202107053>.
- [56] Z. Zhang, J. Sun, F. Wang, L. Dai, Efficient oxygen reduction reaction (ORR) catalysts based on single iron atoms dispersed on a hierarchically structured porous carbon framework, *Angew. Chem. Int. Ed.* 57 (2018) 9038–9043, <https://doi.org/10.1002/anie.201804958>.